



**Report on mechanical boundary conditions and potential
power-electronic architectures
D3.2**

Grant Agreement No.	883553
Start date of Project	1 April 2020
Duration of the Project	48 months
Deliverable Number	D3.2
Deliverable Leader	Uppsala University
Dissemination Level	Public
Version	V1.0
Submission Date	31-03-2022
Author(s)	Johan Abrahamsson, Urban Lundin Uppsala University: Johan.Abrahamsson@angstrom.uu.se Daan Truijen, Jeroen De Kooning Ghent University: Daan.Truijen@UGent.be
Co-author(s)	



The opinions expressed in this document reflect only the author's view and in no way reflect the European Commission's opinions. The European Commission is not responsible for any use that may be made of the information it contains.

This project has received funding from the European Union's Horizon 2020 research and innovation programme under grant agreement No 883553.

Modification Control

Version #	Description	Author	Organisation	Date
0.1	First draft	All authors	UU, Ugent	28-03-2022
1.0	Final version	All authors	UU, Ugent	29-03-2022

Release Approval

Name	Role	Date
Jeroen De Kooning	WP Leader	29-03-2022
Jeremy Bricker	Technical Project Coordinator	29-03-2022
Roelof Moll	Executive Project Coordinator	29-03-2022

History of Changes

Section, page number	Change made	Date

Contents

Executive Summary	6
1 Introduction	8
2 Mechanical fatigue analysis on shaft-driven contra-rotating reversible pump-turbine providing frequency containment reserve	9
2.1 Grid frequency and FCR implementation	10
2.2 Finite element analysis	11
2.3 Machine-side control and surrogate model	12
2.4 Fatigue analysis	14
2.4.1 Simulations	14
2.4.2 Wöhler curve	14
2.4.3 Walkers relation	16
2.4.4 Rainflow counting	17
2.4.5 Fatigue damage accumulation	18
2.5 Conclusion	19
3 Potential power-electronic architectures	21
3.1 Requirements on the drive from the ALPHEUS project	21
3.2 Components of the medium voltage drive	22
3.2.1 The input stage	22
3.2.2 The output stage	23
3.2.3 Control and cooling	23
3.2.4 Example – the ABB ACS6080 motor drive	24
3.3 The inverter	24
3.3.1 Solid-state power semiconductors	25
3.3.2 GTO (Gate turn-off thyristor)	25
3.3.3 IGBT (Insulated-Gate Bipolar Transistor)	26
3.3.4 IGCT (Integrated Gate-Commutated Thyristor)	28
3.3.5 SiC MOSFET (Silicon Carbide MOSFET)	29
3.3.6 SiC Hybrids (IGBTs with SiC diodes)	31
3.4 Topologies	32
3.4.1 Two-level (2L)	33
3.4.2 Neutral Point Clamped (NPC)	34
3.4.3 Cascaded H-bridge (CHB)	35
3.4.4 Flying capacitor (FLC)	35
3.4.5 Quantifying the differences	37
3.5 Vector control techniques	38
3.6 Suppliers	39
3.6.1 INGETEAM	39

3.6.2 Conclusion	42
Conclusion	42
References	46

Nomenclature

f Grid frequency [Hz]

N Number of fatigue cycles [-]

P RPT power [W]

\hat{P} Power setpoint [W]

P_{FCR} FCR capacity [W]

R Quota between minimum and maximum stress [-]

S_{ar} Amplitude of fully reversed stress [MPa]

S_{max} Maximum stress [MPa]

S_{min} Minimum stress [MPa]

t real time [s]

t_0 time at which the power setpoint last changed [s]

γ Walker parameter [-]

σ maximum stress in RPT runner [Pa]

σ_{UTS} Ultimate tensile strength [MPa]

τ_u approximated power step dependent time constant of a first order surrogate model [s/W]

Executive Summary

This report describes the mechanical boundary conditions for full-scale prototype of (primarily) the shaft driven contra-rotating shaftdriven reversible pump-turbine as well as the corresponding power-electronic architectures.

Mechanical boundary conditions

Mechanical fatigue occurs in all systems where a time-varying load is imposed on the mechanical chain. The operating point in electric machines the provide frequency regulation is continuously changing, which results in a changing mechanical stress inside the components. A fatigue analysis of the mechanical parts when providing frequency regulation is therefore of importance in order to ensure that the device is operating within safe limits.

Fatigue is a stochastic property of materials that is normally found by empirical testing. A fully reversed load with no mean component is normally used to specify the material. These conditions are not met in many real-world scenarios of mechanical loading for various reasons, and most certainly not in the case for the ALPHEUS project.

The mechanical stress inside a turbine engaged in frequency regulation is characterized by a static mean component related to the average power the device is generating, and a time-varying component corresponding to the way the device responds to changes in grid frequency. A process was devised in order to convert measurements of grid frequency into corresponding fatigue damage, see Figure 1

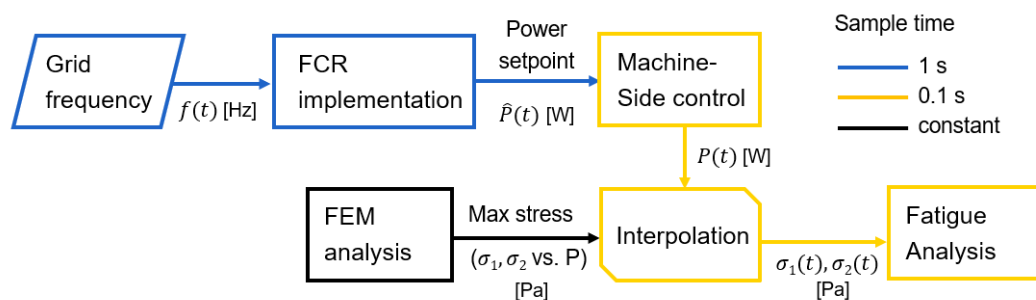


Figure 1: Developed working method for fatigue analysis of the shaftdriven contra-rotating reversible pump turbine providing frequency regulation, with indicated steps, important variables and sample times.

The fatigue in the runner due to the added burden of frequency regulation is potentially a limiting factor for the mechanical parts of the system and should be investigated thoroughly. However, the actual stress levels found in the preliminary design of the test device are not a reason for concern, since they are

much lower than the infinite-life limit and will thereby not cause problems.

For an optimised (perhaps more heavily stressed) design the above evaluation should be performed in order to ensure that the runner is within safe limits. Similar investigations, although out-of-scope for the present investigation, may be required for other parts of the system - e.g. the concrete structure where the stator of the generator is placed.

Power electronic architectures

The world of medium-voltage drives has recently been changing quickly due to the introduction of new power-electronic hardware enabling new topologies and improved control techniques. High-end insulated-gate bipolar transistors are gradually replacing the previously dominating thyristor based systems. As a result, multi-level topologies with advanced control techniques are becoming a standard.

From the investigation into existing technologies for medium voltage drives, it can be seen that commercial off-the-shelf solutions are readily available that would fulfill the needs of the ALPHEUS project. The investigated drives typically handle power-levels of over 10 MW, with a response time of less than 10 ms. Most of them use insulated-gate bipolar transistors in a multilevel configuration with active front-end.

Many suppliers additionally offer the possibility to connect two or more electric machines on the same bus, but they do normally not dimension the active front end considering full generating power, since they typically do this in order to allow machines to share power - when one device is acting as a generator they assume another one is acting as a motor.

When selecting a supplier, care should also be taken to investigate the auxiliary services the provider provides such as help with designing and constructing input and output filters, overvoltage limiter unit on the output (if needed) and breakers (if needed).

1 Introduction

This deliverable documents the work done on boundary conditions for the machine side control as well as suitable power electronic architectures. Especially concerns regarding fatigue loads from the implementation of frequency regulation in the device are considered. The main foci of the deliverable are:

1. Developing a method for estimating the fatigue life of critical components (the runners in particular) given a certain frequency time-series.
2. Documenting the pros and cons of different power electronic components, topologies and control method and investigating their availability and scalability.

Chapter 2 of this document describes the process for estimating fatigue life in the runner. It starts with an overview of the process, after which each step of the process is described in detail.

Chapter 3 in turn describes the requirements from the ALPHEUS project on the drivetrain of the system. An overview of existing and possible future technologies and control techniques are presented.

Note that this deliverable and its results are valid for a preliminary design of the full scale prototype of the contra-Rotating shaftdriven reversible pump turbine. However, the results of Chapter 2 can be readily updated to accommodate for changes in the design or type of prototype (primarily by updating the estimation of stress in the material). The results of chapter 3 are valid for any type of rotating machine design.

2 Mechanical fatigue analysis on shaft-driven contra-rotating reversible pump-turbine providing frequency containment reserve

In this chapter, the mechanical fatigue of the shaft-driven (SD) contra-rotating reversible pump-turbine (CR RPT) providing frequency containment reserve (FCR) is analysed. The fatigue analysis results are then used to ensure that the proposed CR RPT and control architecture work within safe limits. This deliverable provides a detailed working method containing four steps, i.e.:

1. Grid frequency and FCR implementation (section 2.1)
2. Finite element analysis (section 2.2)
3. Machine-side control and surrogate model (section 2.3)
4. Fatigue Analysis (section 2.4)

The working method is depicted in Fig. 6. First, historic grid frequency data is gathered with a sample time of 1 second. Then, an FCR implementation is defined. the FCR implementation comprises the general operation of the RPT and the FCR capacity. Depending on the current frequency $f(t)$, the FCR implementation provides a power setpoint $\hat{P}(t)$. Next, a surrogate model of the machine-side control outputs the physical real-time output power $P(t)$ of the CR RPT. Based on Finite Element Analysis (FEA), a table is formed that includes the maximum mechanical stresses in both runners for certain power points σ_1, σ_2 vs. P . Therefore, using interpolation of these stresses for the current output power $P(t)$ provides real-time max. stresses $\sigma_1(t), \sigma_2(t)$ for further use in fatigue analysis.

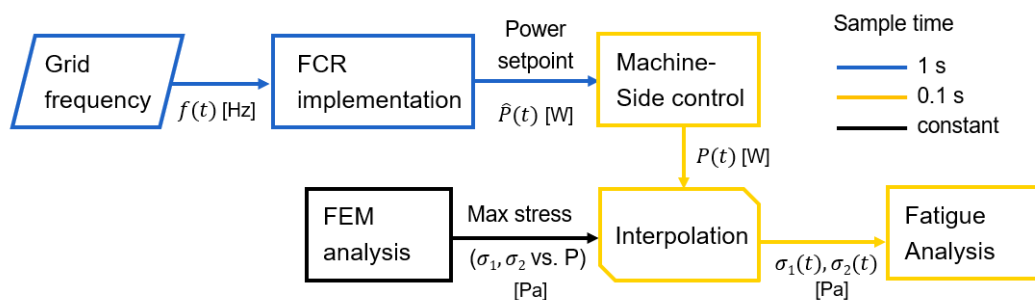


Figure 2: Developed working method for fatigue analysis of the SD CR RPT providing FCR, with indicated steps, important variables and sample times.

In sections 2.1 to 2.4, the different steps to find the mechanical fatigue in the runners are elucidated. Note that this working method provides a procedure

that can be followed if one or more steps are changed in the remainder of this project. For example, if the FCR capacity is increased, the machine power $P(t)$ will change drastically, which causes the fatigue analysis outputs to differ significantly. Another example is the change of runner geometry or material. Here, the FEA simulation and machine-side control will be different and induce other fatigue results. Therefore, the different steps in this working method can be altered and the fatigue analysis can be repeated with the help of the Matlab/Simulink [1] and Python [2] scripts, attached with this deliverable.

2.1 Grid frequency and FCR implementation

In WP6, MS6.1 comprises frequency profiles in Europe, available on the TrasnnetBW website [3]. In this deliverable, the fatigue analysis is performed for system response to available frequency data in 2020, as available in MS6.1. The used frequency data has datapoints per second. Next, the FCR implementation is defined. Here, it is defined how the system responds to the measured frequency at each sample. Note that within the project, outcomes of task 6.2 will define the precise implementation of FCR of the low-head PHS system. In this analysis, the FCR implementation is defined as follows: First, the RPT runs at a power setpoint of $\hat{P} = 5$ MW in either pump or turbine mode. Next, an FCR capacity P_{FCR} is defined at 1 MW. Therefore, if the frequency drops below 50 Hz, the RPT output power setpoint increases to up to $\hat{P} = 6$ MW. Conversely, if the frequency surpasses 50 Hz, the RPT output power setpoint reduces to down to $\hat{P} = 4$ MW. The actual power setpoint is a function of the real-time frequency and is defined as follows [3]:

- When the frequency (f) is within the deadband of 10 mHz ($49.99 \text{ Hz} < f < 50.01 \text{ Hz}$), $\hat{P} = 5$ MW and no FCR is delivered.
- When the frequency (f) drops below 49.99 Hz, or increases above 50.01 Hz, the power setpoint changes linearly with the frequency:

$$\hat{P}(t) = 5\text{MW} - \frac{f(t) - 50\text{Hz}}{0.19\text{Hz}} \cdot P_{\text{FCR}} \quad (1)$$

- When the frequency diverts more than 0.2 Hz from the nominal frequency of 50 Hz, the maximal FCR capacity (+1 MW or -1 MW) is activated.

In equation form this becomes:

$$\hat{P}(t) = \begin{cases} 5\text{MW}, & \text{for } 49.99\text{Hz} < f(t) < 50.01\text{Hz} \\ 5\text{MW} - \frac{f-50\text{Hz}}{0.19\text{Hz}} \cdot P_{\text{FCR}}, & \text{for } 49.8\text{Hz} < f(t) \leq 49.99\text{Hz} \text{ or } 50.01 \leq f(t) < 50.2 \\ 6\text{MW}, & \text{for } f(t) \leq 49.8\text{Hz} \\ 4\text{MW}, & \text{for } 50.2\text{Hz} \leq f(t)\text{Hz} \end{cases} \quad (2)$$

Note that here, also, the FCR implementation can still change within the project. Therefore, it is possible to change e.g. the nominal power of 5 MW and the FCR capacity.

2.2 Finite element analysis

Based on the defined FCR implementation power interval of 4 MW - 6 MW, ADT performed Finite Element Analysis (FEA) on the two runners. Based on five operating points with an output power distributed between 4 MW and 6 MW, the maximum stress in both runners was detected. Table 1 shows the volume flow rate, rotational speeds and torques of these power points, which were achieved by Computational Fluid Dynamics.

Table 1: Operating points for FEA with flow rate, rotational speeds, power and torque.

Total power [MW]	Flow rate [m⁶/s]	Ω_1 [rpm]	Ω_2 [rpm]	T_1 [Nm]	T_2 [Nm]
3.83	94.1	-27	24.3	605001	833116
4.32	97.85	-28	25.2	626337	920476
4.80	101.35	-29	26.1	706337	969721
5.27	104.63	-30	27	749062	1030700
5.84	107.62	-30	27	843165	1129600

FEA is performed using the commercial software Ansys Workbench. Static structural analysis is performed with a single sector of the rotor with cyclic symmetry modelling. The surface pressure on the blades from CFD is extracted and used as the load for the FEA. A cylindrical support is defined and rotational speed is specified for the rotor. Various boundary conditions used are as shown in Fig. 3. Stainless steel (17-4 H1075) is used as the material with the material properties as shown in Table 2.

Table 2: SS 17-4 H1075 Properties.

SS 17-4 H1075 Properties	Value
Density [g/cm ³]	7.89
Young's modulus [GPa]	215
Poisson's ratio	0.33
Tensile yield strength [MPa]	1020
Tensile ultimate strength [MPa]	1130

After the analysis, it is seen that the stresses are well below the material yield

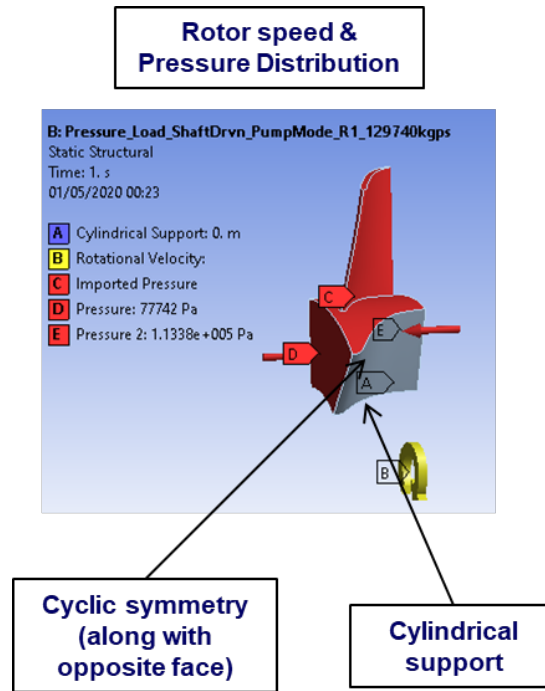


Figure 3: SS 17-4 H1075 Properties.

limit and hence static failure will not occur. The equivalent von-Mises stresses on the blades are plotted as shown in Fig. 4 to identify the high stress region. The maximum stresses for both rotors at various operating conditions shown in Table 3 are used for the fatigue analysis..

Table 3: FEA results for CFD operating points with power and torque.

Total power [MW]	T_1 [Nm]	T_2 [Nm]	σ_1 [MPa]	σ_2 [MPa]
3.83	605001	833116	46.37	55.42
4.32	626337	920476	50.28	60.00
4.80	706337	969721	53.97	64.36
5.27	749062	1030700	57.36	68.49
5.84	843165	1129600	62.49	73.58

2.3 Machine-side control and surrogate model

In work package 3 of the ALPHEUS project, a machine-side control (MSC) is developed that reaches a certain power setpoint \hat{P} as fast and efficiently as possible. Currently, the MSC is under development as according to task 3.5. In this deliverable, the MSC that is applied is a quasi-static lookup table based control algorithm, where the inlet valve angle and the speed of the first runner are controlled in order to reach the power setpoint. The second runner's speed is set at = 90% of the first runner speed. The difference in head between both reservoirs is set at 8 m for this deliverable. The model includes torque control

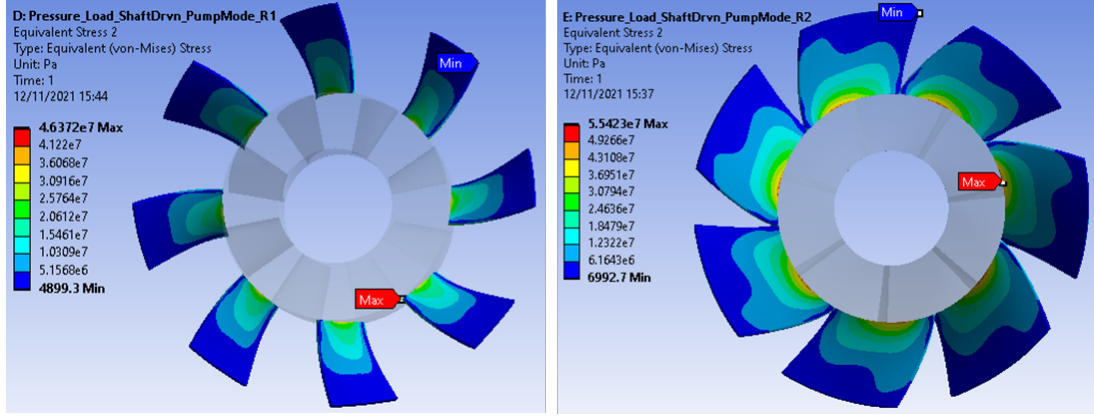


Figure 4: Equivalent von-Mises stress plot on Rotor 1 (left) and Rotor 2 for the first operating point in Table 1.

for both Axial-Flux Permanent Magnet Synchronous Machines (AF-PMSM) as described in Deliverable 3.1 [4].

However, this detailed control model is not suited for fatigue analysis because of its inherently slow simulation times. Therefore, a surrogate model is developed that replicates the dynamic input-output behaviour of the original model while reducing simulation times. In literature, multiple options can be found to create the surrogate model. To allow simple integration of changes in the machine-side control for this fatigue analysis application, a Broïda-based surrogate model is developed. This model reduces the full model to a first-order system with a certain time constant τ . However, it is also possible to replace the existing surrogate model in the Matlab/Simulink script [1] to achieve a higher fidelity model. The used model defines the output power $P(t)$ as follows:

$$P(t) = P(t_0) + (\hat{P}(t) - P(t_0)) \cdot \left(1 - e^{-\left| \frac{t-t_0}{(\hat{P}(t)-P(t_0)) \tau_u} \right|} \right) \quad (3)$$

Here, t_0 is the time at which the power setpoint \hat{P} changes. τ_u [s/W] is the step-dependent time constant that defines the dynamics of the system. This variable can be found by doing a small amount of simulations with the fully detailed control model and analysing the power response $P(t)$ to a step in the power setpoint $\hat{P}(t)$. Then, τ_u can be found as:

$$\tau_u = \frac{\text{time at which } P(t) \text{ reaches } \left[P(t_0) + 63\% \cdot (\hat{P}(t) - P(t_0)) \right]}{\hat{P}(t) - P(t_0)} \quad (4)$$

2.4 Fatigue analysis

Fatigue for a specific material is a stochastic material property that is quantified using controlled experimentation. These experiments are usually performed by applying a fully reversed sinusoidal load with a constant amplitude on a specimen of the material. The specimens are produced with a standardised geometry, ensuring that the resulting stress in the material is known. The fatigue resistance of the material is evaluated by measuring how many cycles the specimen may be exposed to before braking.

Real world fatigue often occurs under very different circumstances. The critical part of the mechanical chain may be exposed to a large constant load in addition to the time-varying load. The time-varying load may not be sinusoidal in nature and may occur sporadically over time. This makes the process of evaluating a certain design with respect to fatigue challenging.

The following sections describe a process for evaluating the extra fatigue resulting from the operation of the ALPHEUS device during participation in frequency control.

2.4.1 Simulations

Initially, 83 hours of the year 2020 were simulated using the surrogate model of the machine-side control. However, after initial analysis of the produced dataset, it was concluded that the response of the machine-side power $P(t)$ to the power setpoint $\hat{P}(t)$ was very dynamic, they followed each other very closely. In Fig. 5, the difference between P and \hat{P} for a certain time interval can be seen. Note that this difference rarely not exceed 0.1 MW which is a very small difference for this estimation.

It can be concluded that for the purposes of fatigue analysis in this specific scenario (comprising RPT geometry and material, FCR implementation and control architecture), the machine-side control does not influence the fatigue analysis. Therefore, it is averted in order to reduce simulation times and increase the time interval that is analysed in this document. Fig. 6 shows the adapted working method that is used for the simulations in this deliverable.

2.4.2 Wöhler curve

August Wöhler (1819-1914) was a German railroad engineer that systematically investigated fatigue failure in railroad axels. He introduced the concept that nowadays is referred to as *Wöhler curves* or *S-N curves*. These curves relate the number of fully reversed sinusoidal load-cycles a certain specimen can endure

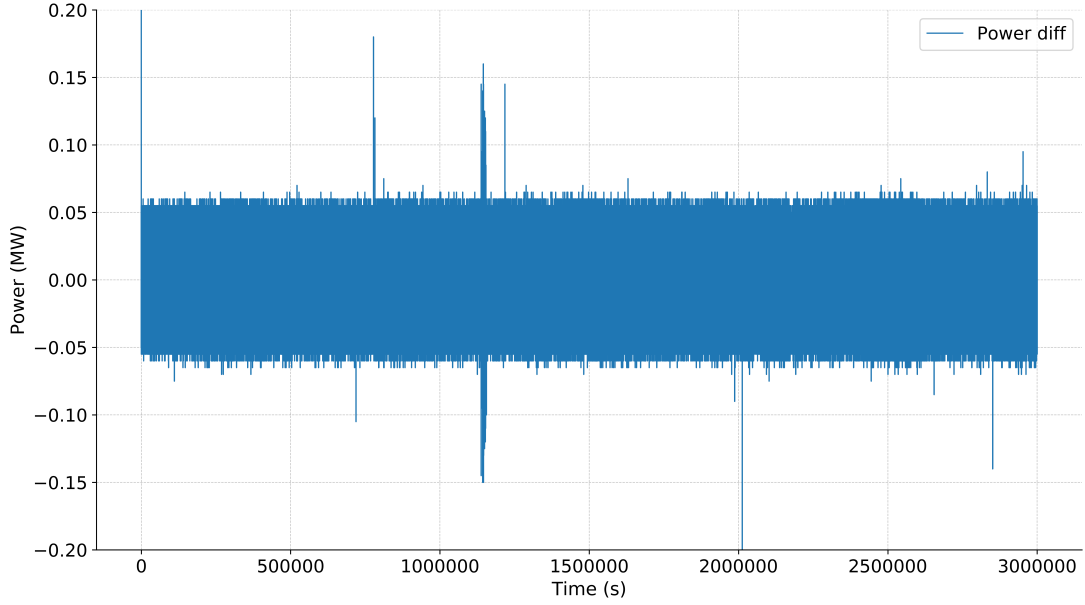


Figure 5: Difference between set-point and response of power.

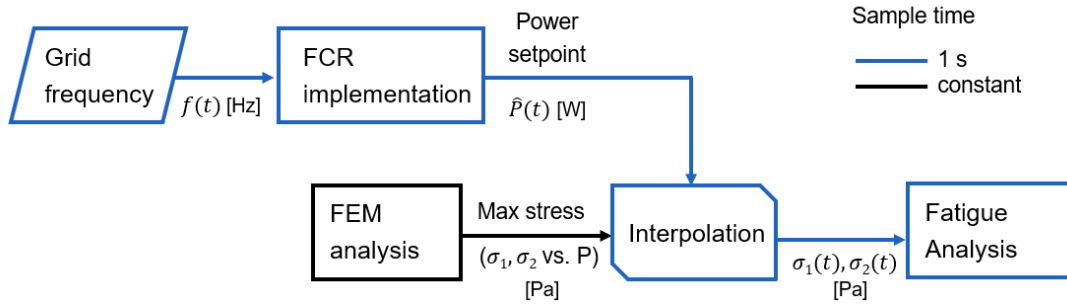


Figure 6: Adapted working method for fatigue analysis of the SD CR RPT providing FCR, averting machine-side control.

before breaking, and can be expressed mathematically as (Basquin's equation)

$$S_{ar} = \sigma'_f N^b, \quad (5)$$

where σ'_f and b are material constants (found empirically), S_{ar} is the amplitude of the fully reversed sinusoidal stress applied, and N is the number of cycles until failure.

The S-N curve for the stainless steel material SS 17-7 PH can be seen in Figure 7. This material has been used in the FEA resulting in the maximum stress in the runner. It can be noted that already at relatively low stress levels fatigue may occur when the specimen is exposed to a sufficient amount of cycles.

For this particular material, σ'_f was estimated to 2374, and b was estimated to

-95.1e-03.

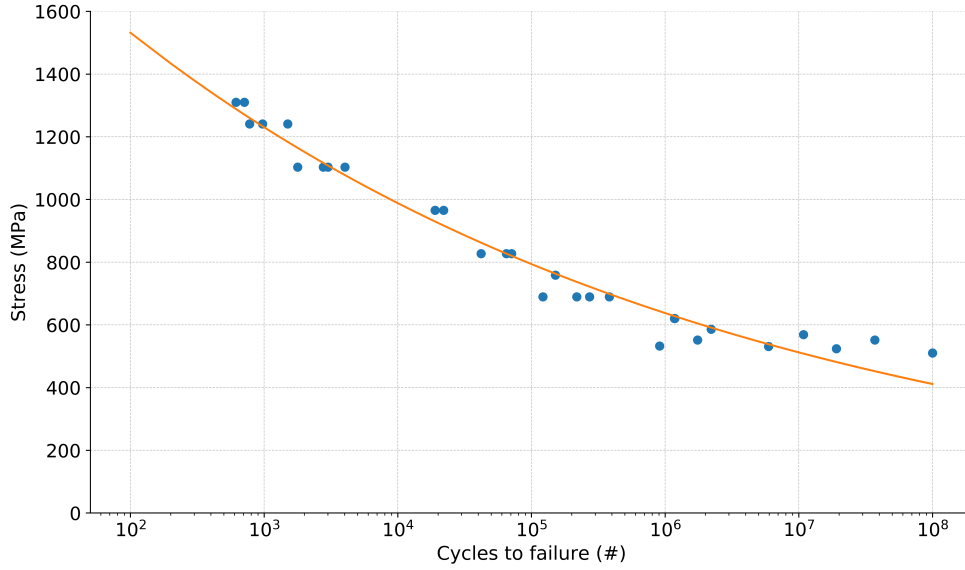


Figure 7: Example of S-N curve from test on SS 17-7. From "Leybold, Herbert A. Axial-load fatigue tests on 17-7 PH stainless steel under constant-amplitude loading. National Aeronautics and Space Administration, 1960."

It can also be noted that under a certain loading, approximately 400 MPa in this case, the material has infinite fatigue life. Loads below this limit will never cause failure, independently of how many cycles are applied.

2.4.3 Walkers relation

The Wöhler curve assumes that the stress in the material is sinusoidal and fully reversed. However, the stress in many real-life applications contains a static component; this is definitively true in the context of the ALPHEUS project.

Various ways of finding the equivalent fully reversed stress (that causes the same fatigue damage as the real stress) has been suggested. One of the most recent approaches is the *Walker relation*

$$S_{ar} = S_{max} \left(\frac{1 - R}{2} \right)^\gamma \quad (6)$$

where S_{max} is the maximum stress a part is exposed to, $R = S_{min}/S_{max}$ is the quota between the minimum stress the part is exposed to and the maximum stress, and γ is a material constant that describes the sensitivity of the material to the mean stress component.

In this context, the parameter S_{ar} can be thought of as the fully reversed stress

profile that would cause fatigue failure after the same amount of cycles as the time varying stress with a mean component that the part is actually exposed to.

The primary benefit of the Walker relation as opposed to simpler relations lies in the material constant γ , which allows the equation to be tuned to measurements of fractional loading. The parameter γ can, in theory, vary between 0 and 1, and describes the resilience of the material to mean stress.

A material with a γ close to 0 is very sensitive to mean stress, whereas a material with a γ close to 1 is very insensitive to the level of mean stress. For steels, the parameter γ can be estimated from the ultimate tensile strength if no measurements of fractional loading exist. The corresponding relation is

$$\gamma = 0.8818 - 0.0002 \cdot \sigma_{UTS}, \quad (7)$$

where σ_{UTS} is expressed in MPa.

For the specific material SS 17-7 PH, the parameter γ becomes 0.60. As can be seen from equation 7, the parameter becomes lower with increasing UTS. This means that the higher the UTS of the material is, the more sensitive it becomes to a mean stress component superposed on the oscillating stress.

2.4.4 Rainflow counting

Another difference between the assumptions of the Wöhler curve and many real-life applications is that they are exposed not to a cyclical load with fixed amplitude, but rather a spectra of amplitudes.

In order to convert a stress time-series with stochastic loads of varying amplitude, an algorithm called *Rainflow counting* was invented in 1968 and has since then been defined in a standard called ASTM E1049-85. The standard contains various specific versions of the algorithm, the one used in this report is the "Pagoda Roof" method.

The fundamental function of the rainflow counting algorithm is to reduce a time-series of stochastic loads into a histogram with a finite number of bins with a defined stress amplitude. The algorithm further extracts the number of cycles each of the bins contain.

As an example of the above methodology, see Figure 8, where two series of stress over time with a significant mean component are depicted. This time-series has been produced by combining the FEA simulations of Chapter 2.2 with the FCR implementation of Chapter 2.1 and extends over one complete year. From the data, the stochastic nature of the stress curve can be appreciated, as well as the large mean stress component.

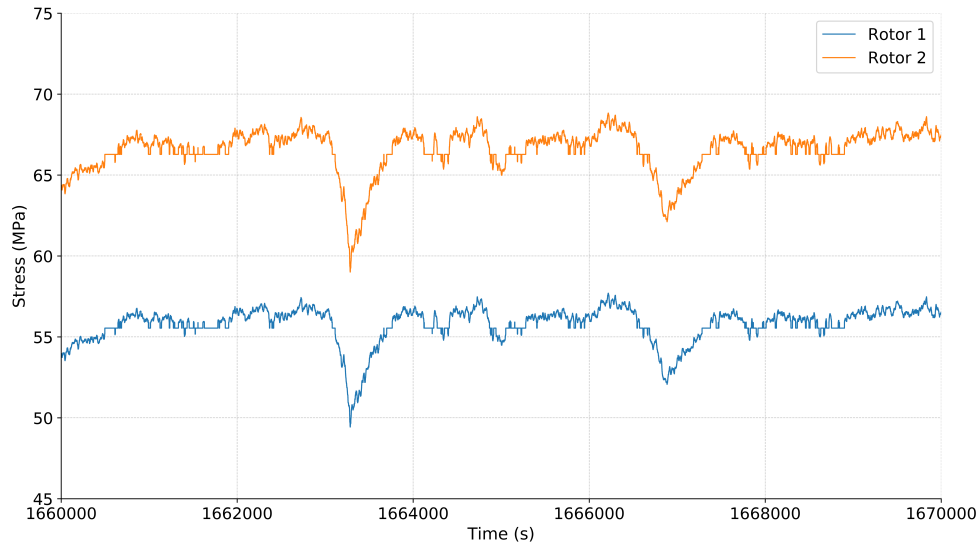


Figure 8: A zoom of the resulting time series of the stress in the point of the runner with highest load during frequency regulation.

By first applying the technique of rainflow counting, the time-varying stress signal is reduced to a histogram showing the number of stress-cycles with a certain binned magnitude. The magnitude of the cycles can thereafter be modified using the Walker relation in order to find the number of fully reversed stress cycles corresponding to the fatigue damage caused by the original data. The results of this process can be found in Figure 9 and Figure 10, for each runner separately.

Each of the bars in the histogram is now readily comparable to the S-N curve of the corresponding material. Naturally, if one of the bars exceeds the limit set by the SN diagram, fatigue failure will occur. Failure normally occurs much before this limit due to the accumulation of fatigue stress caused by all the bars of the histogram. In order to find a realistic estimate of fatigue life, the accumulated damage done by the various stress-ranges has to be assessed.

2.4.5 Fatigue damage accumulation

After the process of the rainflow counting and the correction of the mean stress level using Walkers relation has finished, a finite amount of equivalent fully reversed stress cycles have been found. In order to estimate the cumulative damage that these load-cycles impart, *Miner's rule* can be used.

This equation calculates the remaining fatigue life of a component by comparing the total number of cycles at each stress level with the corresponding number of cycles to failure. The result states how much of the fatigue life that has been

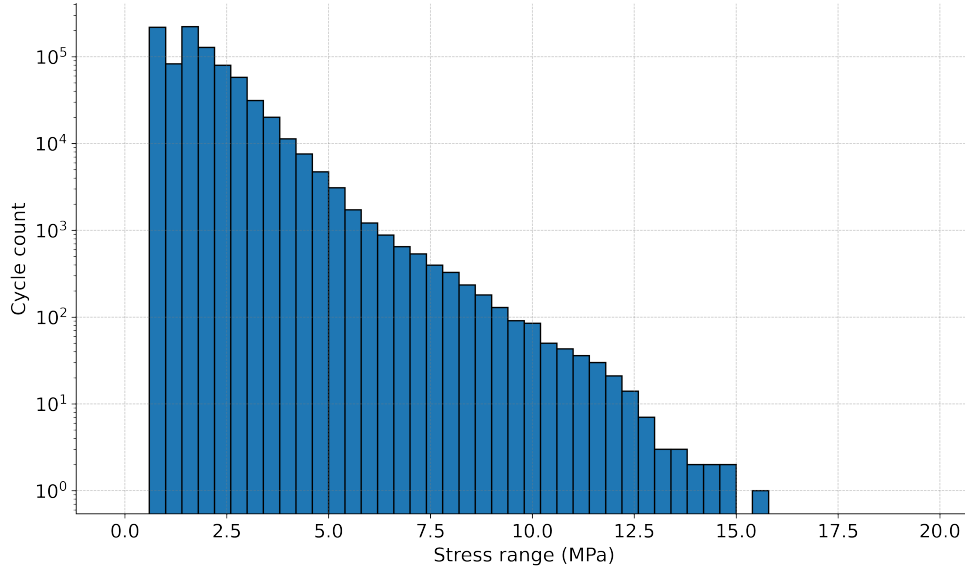


Figure 9: Resulting stress histogram after utilizing the rainflow counting methodology and applying the Walker relation to correct for the mean component of stress. Valid for rotor 1.

consumed, see Equation 8

$$C = \sum_{i=1}^k \frac{n_i}{N_i}, \quad (8)$$

where C is the fraction of fatigue life consumed, n_i is the number of cycles at stress level S_i , and N_i is the number of cycles to failure at stress level S_i .

For the test-device being investigated, this last step is not required since the resulting stress levels are lower than the infinite life of the material. This implies that the additional fatigue stress caused by participation in grid frequency regulation under the assumptions of geometry and participation level is negligible and that no further calculations are necessary (the parameters N_i in Equation 8 becomes infinity).

2.5 Conclusion

The fatigue in the runner due to the added burden of FCR is potentially a limiting factor for the mechanical parts of the system and should be investigated thoroughly. The stress levels found in the design of the test device are not a reason for concern, since they are much lower than the infinite-life limit and will thereby not cause problems. For an optimised design, which perhaps is more heavily stressed, the above evaluation should be performed in order to ensure that the runner is within safe limits.

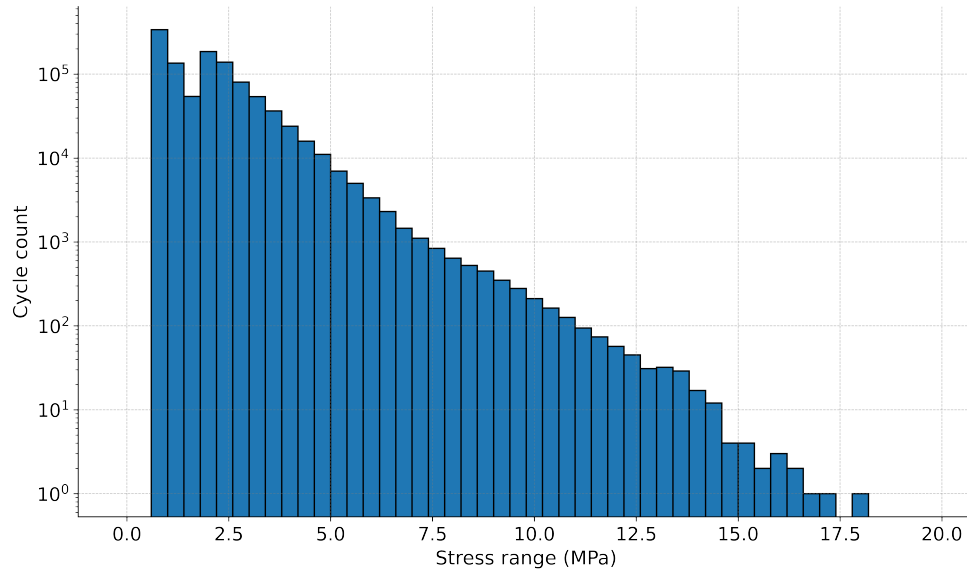


Figure 10: Resulting stress histogram after utilizing the rainflow counting methodology and applying the Walker relation to correct for the mean component of stress. Valid for rotor 2.

When the fatigue analysis in this evaluation does not comply with the aimed lifetime of the RPT, two main design feedbacks are foreseen. First, using a pump-turbine material with higher yield strength can increase fatigue life. However, in cases when RPT design is final, this solution is not possible. Next, the machine-side control ramp rates for reaching the power setpoint can be altered. Note that, although a straight-forward implementation, the decrease in dynamic response of the machine-side control can have implications on the ability to provide FCR.

Similar investigations, although out-of-scope for the present investigation, may be required for other parts of the system - e.g. the concrete structure where the stator of the generator is placed.

3 Potential power-electronic architectures

Medium voltage (MV) drives are typically defined as operating in a range from a 200 kW up to 40 MW at voltage levels between 2.3–13.8 kV although the bulk of installed drives in the world are in the range of 1–4 MW and with voltage ratings of 3.3–6.6 kV. They are used in a large number of industrial settings; oil and gas, petrochemical, renewable power generation, traction and marine to name a few and the yearly number of installed systems has been increasing steadily around 10 % on a year-to-year basis [5].

The last decades have seen significant advances of the power semiconductors used in these systems, which in turn has resulted in various utilised topologies. The presently commercially available MV drives use one of three different technological platforms

- Voltage-Source Inverters (VSI)
- Current-Source Inverters (CSI)
- Cycloconverters (CC)

All three types of drives are capable of driving synchronous electric machines, but differ in the type of switching technology used (the semiconductors), modulation technique as well as resulting topology. Not all of these three types of drives are ideally suited for all types of machines; differences exist when it comes to maximum power, maximum voltage, efficiency as well as required maximum output frequency.

In the medium voltage segment, the current-source inverters as well as cycloconverters are gradually being phased out due to the complex and costly hardware and limited control [6]. Therefore, the following document will focus on the VSI since they are considered the most relevant for future installations.

3.1 Requirements on the drive from the ALPHEUS project

The ALPHEUS project has as overarching aim to show the viability of improving grid stability by using low head pumped hydropower. To this end, an innovative full scale unit comprising two counter-rotating turbines connected to two permanent magnet synchronous machines (PMSM) has been suggested. For a detailed description of the system under consideration, see [7].

Improving grid stability implies regulating the power consumption / production of the unit in real-time as a function of grid frequency. Summarizing the requirements on the drive yields the following list of desired properties the drive(s) should fulfill

- At least 6 MW per unit, in generator- as well as motoring mode
- At least 10 MW to grid bidirectionally
- Vector control of permanent synchronous magnet machines
- Fast control action, separate for each of the two PMSM
- Reactive power control towards the grid

3.2 Components of the medium voltage drive

For an overview of the components of the drive, see Figure 11 and the following sections.

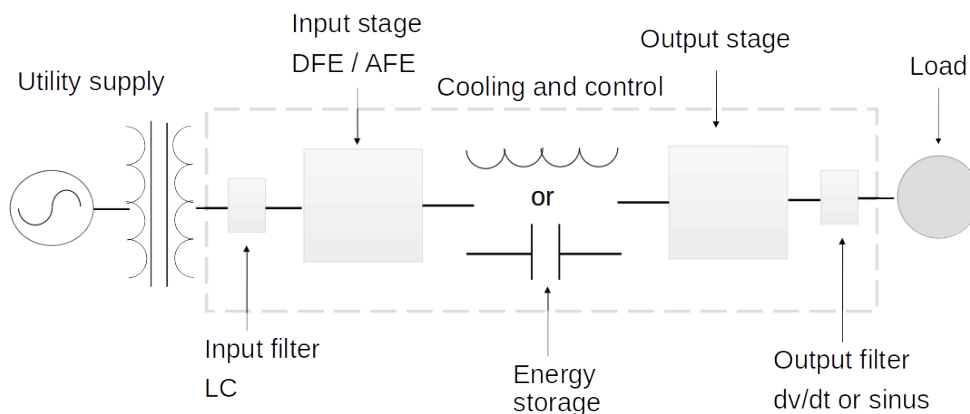


Figure 11: Main components of a medium voltage drive.

3.2.1 The input stage

The input stage of the drive typically consists of either a passive diode rectifier (Diode Front-End, DFE) or a switched converter (Active Front-End, AFE). The AFE is constructed from controllable power semiconductors and allows the drive to operate in 4Q mode, sending power back to the grid when the machine acts as a generator, but also increases the cost of the drive significantly (typically by almost a factor of two).

The DFEs in particular create a large amount of harmonics on the utility side. The amount of allowed harmonics is defined in the standards and corresponding input filters (LC or L) are normally required. These filters need to be dimensioned with care since they may cause oscillations or overvoltages under certain conditions. The AFE typically produces much less harmonics, and thereby enables the use of smaller input filters.

The energy passing through the input stage is stored in an intermediate energy storage (inductive for CSI and capacitive for VSI).

3.2.2 The output stage

The output stage of the drive formats the energy in the intermediate storage to a shape and magnitude optimised for the load at any given moment in time. The output stage consists of controllable power semiconductors in one of various possible configurations; which configuration that is chosen depends to a large extent on the type of semiconductor in use.

The fast switching action of modern power semiconductors cause high voltage stress on the insulation of the motor. Long motor cables worsen this effect, and can cause a doubling of the voltage on the motor terminal each time a switch is actuated. Additionally, high frequency common-mode voltages on the motor cables may cause bearing failure over time. To mitigate these issues, an output filter is normally placed between the output stage and the load.

The output filter may be of a smaller type (dv/dt) which only reduces the steepness of the voltage front coming from the switches, or a larger type (sinus) which also formats the resulting current from the drive into a sinusoidal shape with little harmonic content. The dv/dt filter is typically chosen for newer motors and the sinus filter for older ones.

3.2.3 Control and cooling

The control of the drive ensures that the motor is operated in an efficient way. This typically means some form of vector control, either with the input of an encoder on the shaft or sensorless. The exact algorithm used to produce the PWM action may additionally help to mitigate voltage stress, reduce harmonics and/or reduce common mode voltage in the load. The control may also be able to provide both active and reactive power to the grid in case the input stage is an AFE.

Finally, in order to ensure the longevity of the components of the drive, proper cooling is required. Much effort goes into optimizing the layout of the components in the cabinet to make sure that no hotspots occur. The drives are typically air-cooled (forced) for lower ratings and water-cooled for higher ratings.

3.2.4 Example – the ABB ACS6080 motor drive

A concrete example of the layout of a medium voltage drive (the ABB, ACS6080) can be found in Figure 12. It shows the parts of the drive, with the cabinets housing the AFE and the (identical) inverter unit opened. This particular drive uses the a switching technology called IGCT thyristors, and a three-level configuration neutral point clamped topology (more on this later on).

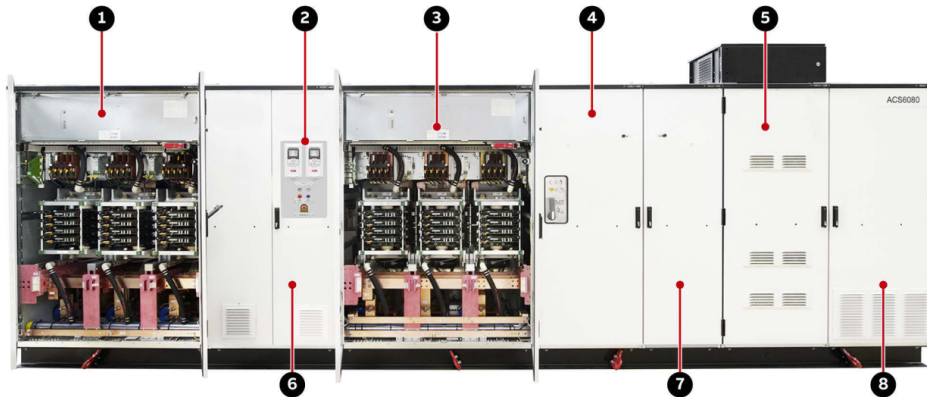


Figure 3-2 ACS6080 drive example

1) Active rectifier unit (ARU): Self-commutated, 6-pulse, 3-level voltage source inverter with IGCT technology	5) Water cooling unit (WCU): Supplies deionized water for cooling the main power components
2) Drive control panel for local operation: Keypad with multi-language display, main supply on/off push buttons, and emergency-off push button	6) Terminal unit (TEU) and control unit (COU): Contains the power terminals and the control swing frame
3) Inverter unit (INU): Self-commutated, 6-pulse, 3-level voltage source inverter with IGCT technology	7) Braking chopper unit (BCU), resistor braking unit (RBU) or voltage limiter unit (VLU): Optional cabinet units
4) Capacitor bank unit (CBU): DC capacitors for smoothing the intermediate DC voltage	8) Excitation unit (EXU): Optional cabinet unit that supplies a synchronous motor with excitation

Figure 12: n example of a complete medium voltage drive, the ACS6080 from ABB. Picture from [8].

3.3 The inverter

Before looking into the concrete offerings of medium-voltage drives on the market, it is instructive to go a bit deeper into the technology of the inverter. The input and output stages of modern MV drives comprise a number of power semiconductors, connected together in certain topologies. The properties of these semiconductors define many other parameters of the drive, such as its efficiency, how much cooling is needed, and which filters to use.

3.3.1 Solid-state power semiconductors

The solid-state controllable power semiconductors used in MV drives can broadly be categorised in two families; *transistors* and *thyristors*. The performance of these devices has increased drastically during the years, primarily driven by inventions of new devices but also improvements in the manufacturing (the purity of the doping) of the semiconducting material and the devices themselves [9], [10].

Members of the thyristor family have been used in converters since the 1960s. They have a relatively simple internal structure and can readily be implemented on wafers of varying size. Notable members of this family include the **SCR** (Silicon controlled rectifier), **GTO** (Gate turn-off thyristor), **IGCT** (Integrated Gate-Commutated Thyristor), **ETO** (Emitter turn off thyristor) and the **SGCT** (Symmetric Gate-Commutated Thyristor).

Members of the transistor family are more complex, but have become dominant in the low- and medium voltage range in the last decades due to continuous improvements. Notable members of this family are the **BJT** (Bipolar Junction Transistor), **Power MOSFET** (Metal Oxide Semiconductor Field Effect Transistor), and most significantly the **IGBT** (Insulated-gate bipolar transistor).

For a rough timeline of their introduction, see Figure 13.

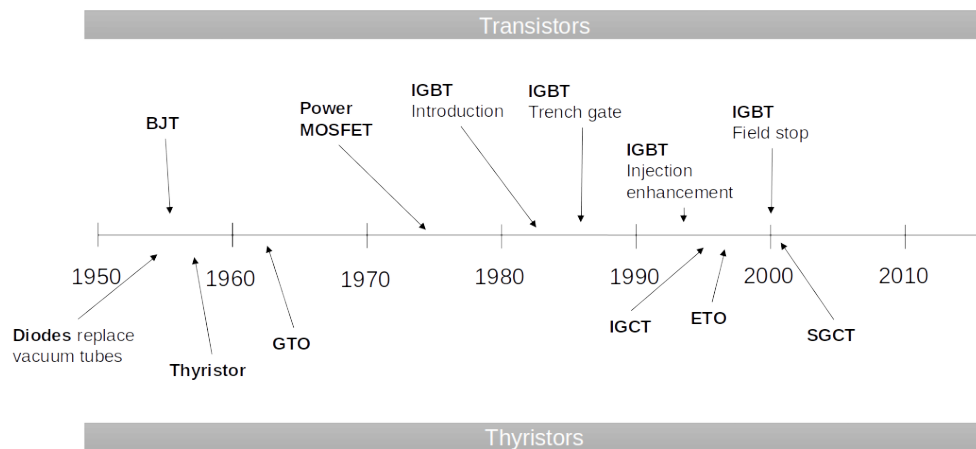


Figure 13: Introduction of solid-state power semiconductors, data from [9].

The following sections describe briefly the properties of a few selected technologies, which are still in use today.

3.3.2 GTO (Gate turn-off thyristor)

The GTO is a type of semiconductor device invented by General Electric made available in 1962 and still in use. It is an evolution of the Silicon Controlled

Rectifier (SCR, introduced by GE at the end of the 1950s) that unlike the SCR can be turned off using its gate [11]. However, this technology comes with a number of drawbacks

- It requires high current from the gate driver
- There is a significant delay between the turn-off command and the actual reaction of the device (up to 50 μ s)
- Because of its large size, snubber inductors are required for the current to spread evenly through the die
- It has poor turn-off characteristic, which requires large snubber capacitors

These drawbacks result in a switch with a complex driver circuit, high switching loss and long delay times. Switching frequencies are typically 200–500 Hz, see Figure 14.

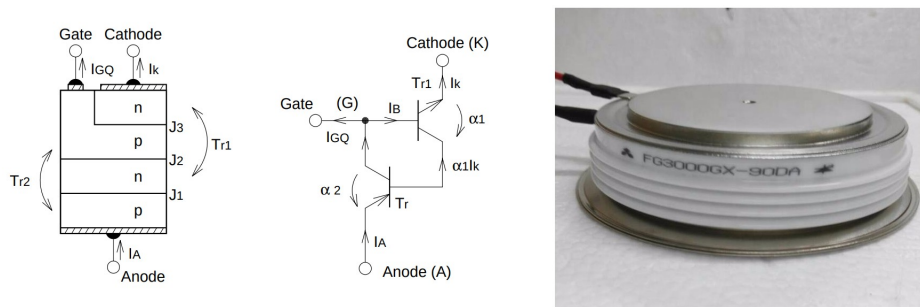


Figure 14: Internal structure and picture of the Mitsubishi FG3000GX-90DA GTO, rated for 4.5 kV and 3.6 kA [12].

The GTO is in general considered mature and proven technology. It was dominating the market during the 1980s and most of the 1990s, and is still sold today for applications such as variable speed motor drives, but has in new designs generally been replaced by IGBTs and IGCTs.

3.3.3 IGBT (Insulated-Gate Bipolar Transistor)

In parallel with the development on the thyristor side, the IGBT was introduced in the 1980s as a development of the Bipolar junction Transistor (BJT).

The BJT had severe drawbacks with low current gain resulting in very large devices, as well as requiring snubber circuits. During the 1970s, the power MOS-FET had been introduced for lower voltage and current ratings. The IGBT solved many of these issues by combining the modes of operation of the power

MOSFET with that of the bipolar transistor, resulting in high impedance voltage controlled operation.

The IGBT was limited at the beginning with slow switching times and limited safe area of operation. However, improvements of the technology such as the *trench-gate*, the *injection enhancement effect* and the *field-stop layer* gradually increased the usability of the device over time by increasing switching speed, decreasing the forward voltage drop and increasing the safe area of operation [13].

The trench gate structure (1987) was suggested by Chang et.al. (GE). By fabricating the device using vertical trenches, the channel density was increased and the forward voltage drop reduced. It also removed the so called parasitic JFET effect which up till then had placed limitations on the maximum current density the device could handle [14].

The injection enhancement effect (1993), as described by Kitagawa et.al. (Toshiba), resulted in a power device with similar forward drop as the GTO, while still retaining its turn-off capabilities. This was achieved by optimizing the MOS-gate in the IGBT in such a way that the carrier distribution in the material became similar to that of a thyristor. In this way, the blocking capabilities (given a reasonable forward voltage drop) was significantly increased [15].

The field stop IGBT (2000), described by Laska et.al. (Infineon), added a thin, weakly doped, layer to the IGBT with the sole purpose of stopping the electric field under blocking conditions. This, in combination with the aforementioned trench structure resulted in an optimised carrier concentration, which in turn reduced the size of the IGBT with a factor of three while at the same time reducing the on state voltage and reducing dynamic losses [16].

During the last decade, the IGBT has become the dominant power device both in the low- as well as the medium-voltage drive segment. Individual IGBT modules exist off-the-shelf with voltage class up to 6.5 kV, and maximum rated currents up to 3.6 kA, the latter typically achieved by placing two or more IGBTs in parallel inside the package. For an overview of presently commercially available modules from three selected suppliers, see Figure 15.

An example of such a power module, which also serves to illustrate the efforts of the suppliers to continuously improve the IGBT technology can be seen in Figure 16. The *CM1800HC-66X* from Mitsubishi consists internally of three IGBT units connected in parallel and controlled by the same gate signal and is rated for 1.8 kA and 3.3 kV.

This device is a 7th generation HVIGBT (announced in 2016) and features significant reduction in both turn-off energy, forward voltage drop as well as increased ability for power cycling compared with the 6th generation (released in 2009), [20]. Similar progress is also made by the other suppliers of IGBTs.

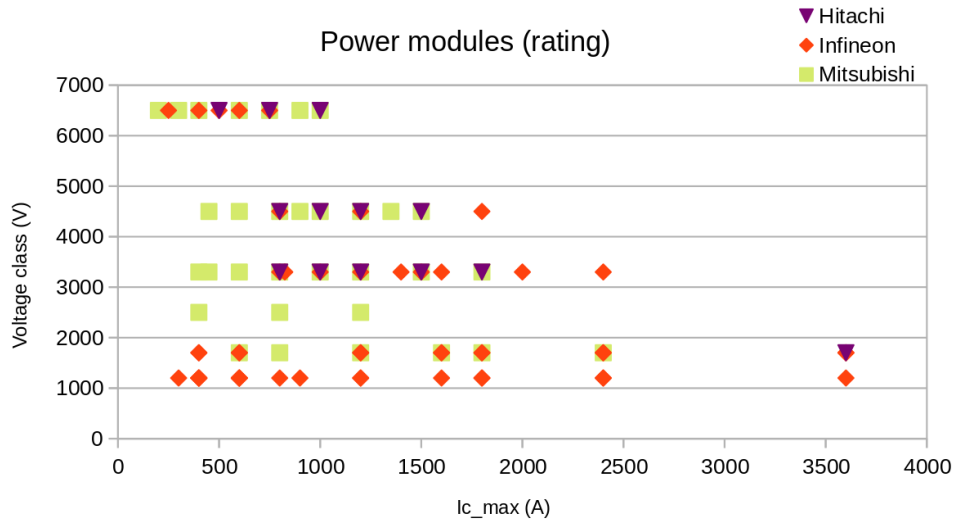


Figure 15: Overview of power rating of IGBT modules (2021), data from [17], [18] and [19].

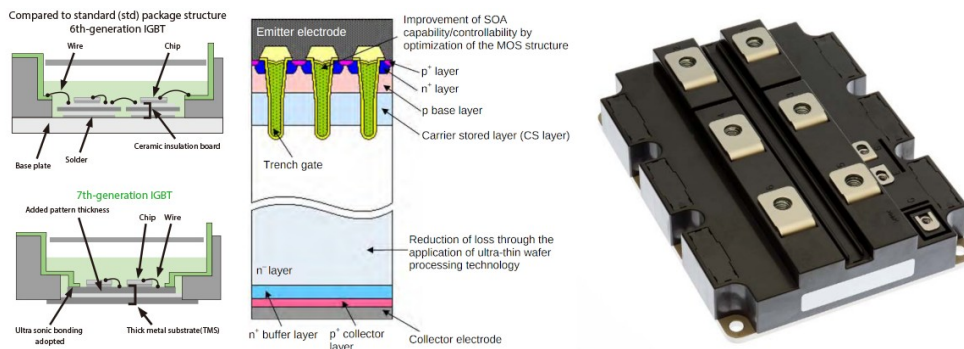


Figure 16: Power module CM1800HC-66X from Mitsubishi Electric, [20] and [21].

3.3.4 IGCT (Integrated Gate-Commutated Thyristor)

The IGCT is a type of power semiconductor that was developed by ABB during the 1990s. It was created as a means to improve on the existing GTO design, reducing the need for costly dv/dt - and di/dt -snubber circuits and as well as decreasing the cost of the gate drive units [22].

The IGCT takes advantage of the excellent conduction properties of the thyristor, while acting as a transistor during turn-off and blocking conditions. Shortly before turning off, the switch changes from a thyristor-based structure to a transistor-based structure by commutation of the cathode current, see Figure 17. In this way, the device resembles a thyristor while conducting, but an IGBT while blocking [23], [24].

Both IGCTs and IGBTs are presently used in medium voltage drives with similar

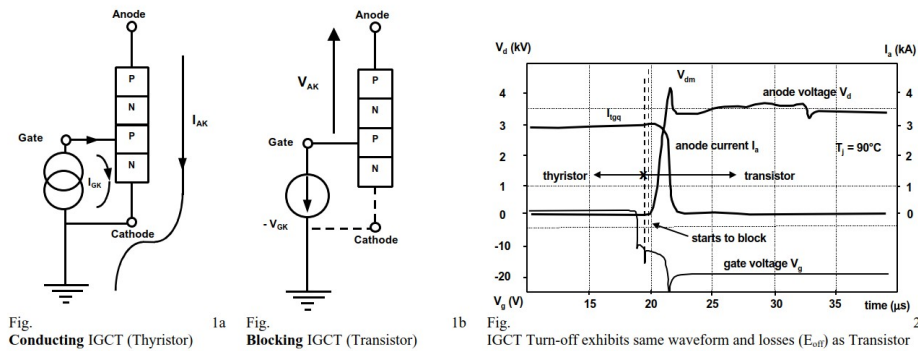


Figure 17: Function of the IGCT. The device changes from a thyristor based structure to a transistor based on shortly before turning off, from [22].

topologies. One drawback of the IGCT compared with the IGBT is the very high gate current needed to turn off the IGCT – in the order of several thousand Ampere. These pulses are very short, but requires a relatively complex driver with a significant amount of electrolytic capacitors on the driver board, see Figure 18.

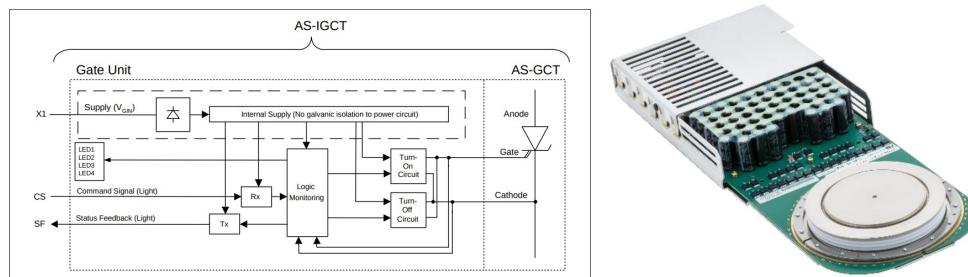


Figure 18: Asymmetric IGCT from Hitachi / ABB for 6.5 kA and 4.5 kV [25].

Typically, the forward voltage drop of a IGCT is lower than that of the corresponding IGBT, but the switching losses are higher. On the other hand, the driver circuit of the IGCT is more complex and prone to failure, while the semiconductor itself is simpler and less prone to failure.

However, it should be noted that these differences may sometimes be small enough to not really impact the final product and additionally there is extensive continuous development of both technologies, making a fair comparison between the two a moving target.

3.3.5 SiC MOSFET (Silicon Carbide MOSFET)

Semiconducting materials come in many varieties – all the ones discussed so far have been based on silicon. However, this was not always the case...

In the end of the 1950s, industrial semiconducting transistors were typically made from high purity germanium, although silicon based systems existed. The annual sales of germanium diodes outnumbered the silicon based ones with at least an order of magnitude. The same goes for price - silicon based transistors were an order of magnitude more expensive than the germanium based ones. However, already at the end of the 1960s silicon had become the material of choice for producers of semiconductors, and this has remained so until the present day. The shift from using germanium to embracing silicon was quick and abrupt.

Silicon has a higher band gap than germanium – this means that it has higher blocking voltage and can operated at higher temperatures. It also has higher thermal conductivity, implying that the heat generated in the junction of the switch can more easily be transported out of the semiconducting material. Last, but not least, a technique was found to stabilize the surface of the silicon devices using a thin layer of silicon dioxide leading to the planar process manufacturing technique that revolutionised the production of semiconducting devices (no similar process was ever found for germanium) [26].

A similar process could be happening right now. In the last decades, a new material – silicon carbide – has been proposed and refined into functioning power semiconducting devices. SiC has a wider band gap than silicon (with almost a factor of three) and is very dense, leading to devices that can operate a high temperatures, has high thermal conductivity and very high dielectric breakdown field (an order of magnitude better than Si) [27].

For an overview of the fundamental differences between SiC and Si, see Figure 19.

Property	Unit	Si	4 H-SiC	6H-SiC	3C-SiC	GaN	GaAs	Diamond
Bandgap	eV	1.12	3.26	3.02	2.23	3.39	1.43	5.47
Electron mobility μ_e	cm ² /Vs	1400	1000 ↓ to c-axis 1200 to c-axis	450 ↓ to c-axis 100 to c-axis	1000	900	8500	2200
Hole mobility μ_h		600	120	100	50	150	400	1600
Electric breakdown field E_c	V/cm	3.0×10^5	2.8×10^6	3.0×10^6	1.5×10^6	3.3×10^6	4.0×10^5	1.0×10^7
Thermal conductivity λ	W/cmK	1.5	4.9	4.9	4.9	2.0	0.5	20
Saturated electron drift velocity V_{sat}	cm/s	1.0×10^7	2.2×10^7	1.9×10^7	2.7×10^7	2.7×10^7	2.0×10^7	2.7×10^7
Relative dielectric constant ϵ		11.8	9.7 ↓ to c-axis 10.2 to c-axis	9.7 ↓ to c-axis 10.2 to c-axis	9.7	9.0	12.8	5.5

Figure 19: Physical properties of semiconductor materials, from [27].

SiC Mosfet based power modules for up to 1.7 kV and several hundreds of Ampere do already exist, but they are significantly more expensive then their IGBT based counterparts at the moment. As an example, see Figure 20 showing a comparison between two power modules (half bridge configuration), the first one is a SiC MOSFET and the second an Si IGBT semiconductor. Both modules are rated at approximately 400 A, 1.2 kV.

Although the SiC MOSFET undoubtedly provides benefits and potential effi-

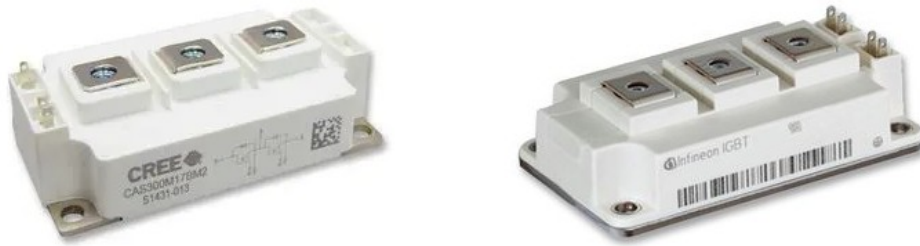


Figure 20: Comparison of SiC and IGBT power modules (half-bridge). Left: The CAS300M12BM2 (SiC) from Wolfspeed, 400 A, 1.2 kV, 567 Euro. Right: the FF300R12KT4HOSA1 (IGBT) from Infineon, 136 Euro. (Prices from Farnell, 13/10 2021).

efficiency gains compared with traditional IGBTs, care should be taken when quantifying these benefits. In [28] such a comparison was made for a 20 kW inverter operated at 800 V, with overall efficiency in mind. The efficiency of the SiC based system was always greater than the IGBT based system, but marginally so for switching frequencies below 20 kHz. The SiC system was, as to be expected, found to have much lower switching losses than the IGBT based system.

Another important aspect to consider when comparing these two technologies is reliability. In [29] an evaluation of reliability during power cycling was performed. 18 MOSFET based SiC switches in the TO-247 package were evaluated and compared with a reference IGBT switch. From the results, the large variability in the degradation of the SiC switches can be highlighted, with one sample surviving 200 000 cycles without noticeable degradation, while another failed after only 8600 cycles. This could be an indication of a technology with great potential but with a continued need to improve quality control during manufacturing.

3.3.6 SiC Hybrids (IGBTs with SiC diodes)

SiC diodes have, unlike their MOSFET counterparts, already found their way into the world of medium voltage drives. The IGBT always blocks current conduction in the reverse direction, and therefore needs an anti-parallel diode placed over the switch in order to provide a current path during switching transients. This diode conducts every time the switch changes state, incurring significant losses.

In order to reduce these losses, diodes made from SiC have started to find their way into the medium voltage converters. In [30], Toshiba presents its hybrid solution with a silicon carbide Schottky barrier diode – the SiC version of this type of diode offers much higher reverse voltage (up to 1700 V) compared with its silicon counterpart. The fast reverse recovery time of the Schottky diode leads

to a reduction of losses in the inverter, see Figure 21.

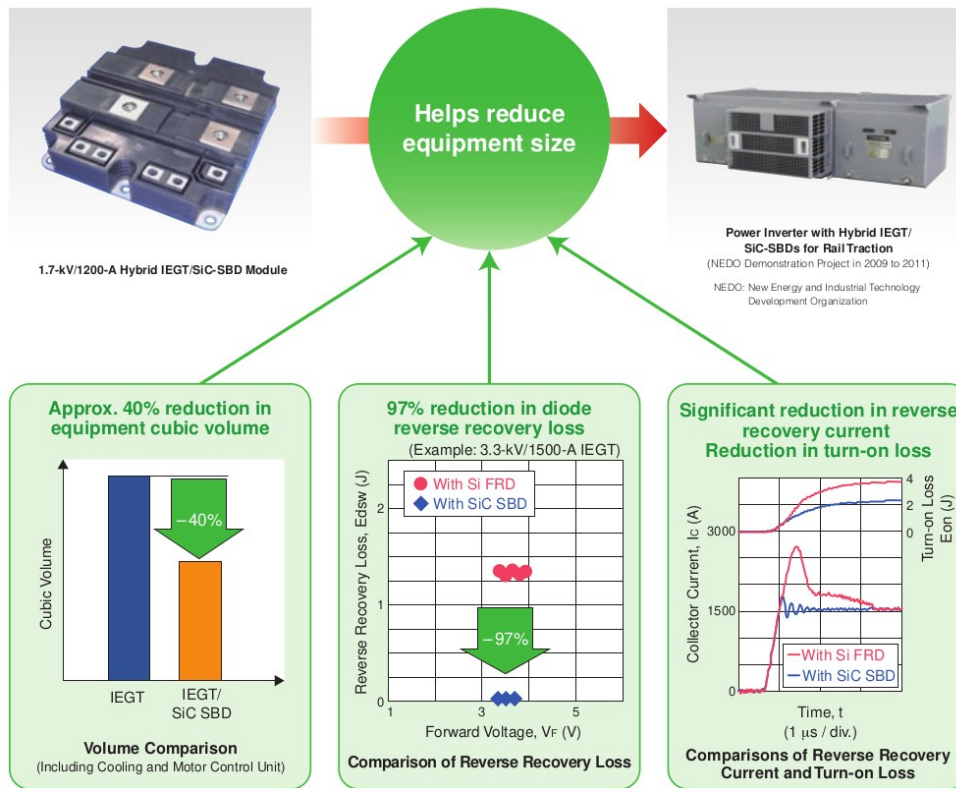


Figure 21: SiC Schottky diodes with very fast reverse recovery help to reduce losses, heat and volume of power inverters. Picture from [30].

In [31] the benefits of the hybrid system described above was quantified in the form of a traction inverter (1.5kV DC link) for a train car. Without changing the cooling system, the SiC diodes helped reduce the total continuous losses in the inverter during operation with 3%, and increase the capacity of the inverter to regenerate braking energy with 28%.

3.4 Topologies

In parallel with the development of semiconductors seen in the previous sections, also new modulation techniques (used to control them) have been found. This has led to several different viable topologies – ways these switches can be assembled and controlled – each one optimised for its own particular application.

The following sections discuss the most relevant of these topologies for the Alpheus project (the information in the following sections is based on [32]).

3.4.1 Two-level (2L)

The traditional two-level inverter structure can be extended to higher power levels by placing several switches in series. Considering that each switch could be rated for 6.5 kV, this would enable such a topology to cover the voltage range of the medium voltage drives, see Figure 22.

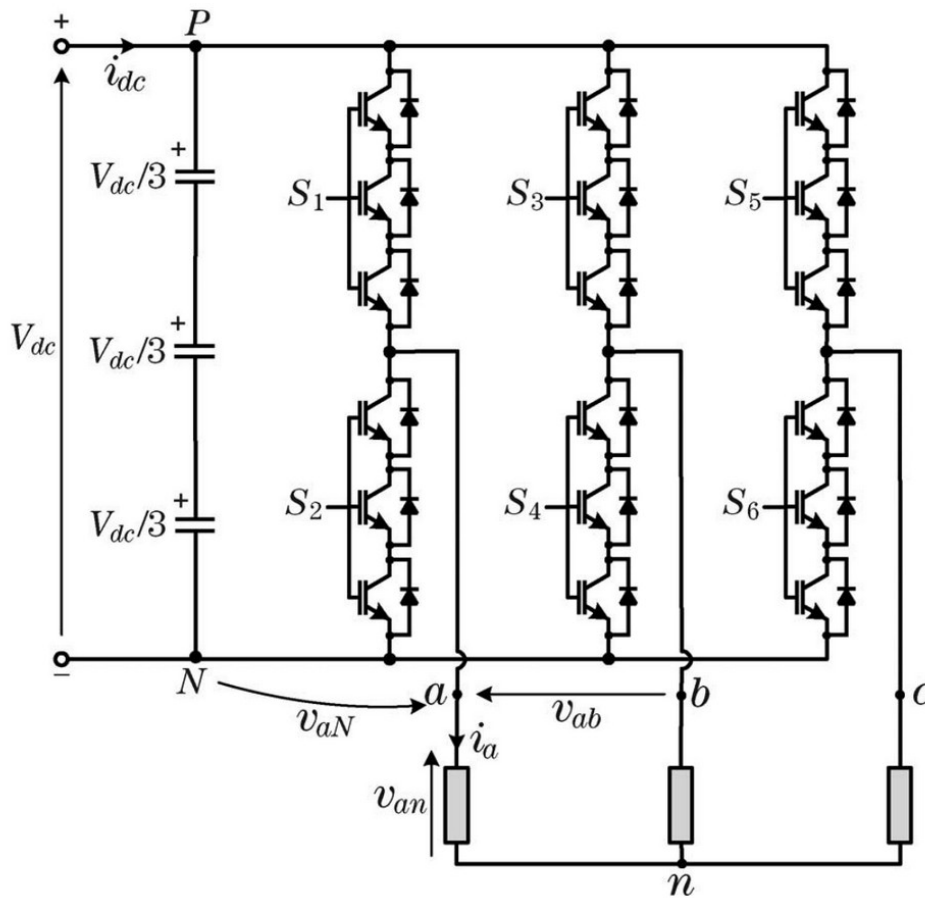


Figure 22: Two-level (2-L) circuit. Picture from [32].

However, simple as this topology may be, it comes with drawbacks. The very high DC link voltage may require the capacitors of the bank to be placed in series. Both input and output harmonics are high, and the transient voltage stress on the load when switching may be detrimental. To this end, most producers of medium voltage drives take advantage of one of the more advanced topologies, the so-called multi-level inverters.

3.4.2 Neutral Point Clamped (NPC)

The NPC was developed in the 1980s and offered a relatively simple way to expand the power level of existing 2L inverters. In a three-level NPC, each switching element operates at half the dc-link voltage, and the only additional elements required are six diodes. These additional diodes link the neutral point of the device to the midpoint of the series connected switches, allowing also the neutral point of the inverter to be connected to the output. A typical circuit of a three-level NPC inverter can be seen in Figure 23.

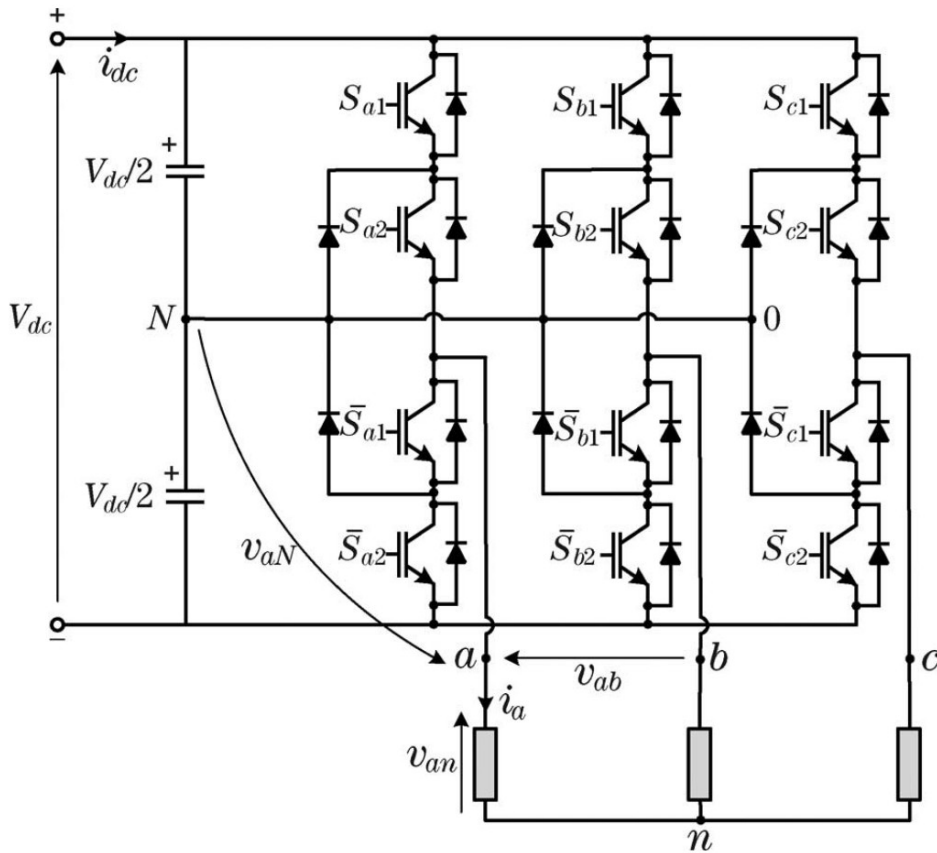


Figure 23: Three-level circuit with clamped neutral point. Picture from [32].

When controlling the NPC, care must be taken not to place the system in a state which leads to destruction of the device. This can happen either by exposing an individual switch to the full dc-link voltage, or by short circuiting the capacitor bank. To this end, the four switches in each leg are controlled as anti-parallel pairs. When switch S_{a1} in the figure above is turned on, the complementary switch \bar{S}_{a1} must be turned off, and the same goes for the rest of the switches.

Under these constraints, 27 possible switch-states remain (some overlapping) yielding 19 unique states of the inverter. This makes it possible to build-up an

output signal with significantly lower THD than the corresponding 2L inverter can. Further, the overlapping states can to some extent be used to control the voltage level of the two series-connected capacitor banks, which is required in order to keep the potential of the neutral point constant.

The 3L NPC topology with the corresponding control is considered mature technology and has been widely adopted by industry both for application as motor control as well as for the active front-end. It is currently the most widely implemented multi-level topology in industry. One example is the ABB ACS6080 mentioned in the introduction.

The biggest drawback with this topology is that it does not scale easily; for inverters with more than three levels, problems arise with unequal semiconductor losses and voltage balancing. However, it is well suited in particular for the mid-to lower end of the medium voltage drive segment, where three levels are enough.

3.4.3 Cascaded H-bridge (CHB)

The cascaded H-bridge was developed during the early 1990s, and consists of a larger number of power cells, comprising electrically isolated 2L H-bridges. The electrical isolation can be achieved by using a multipulse transformer. A certain number of such power cells are connected in series, making it possible to generate a large number of different output levels, especially if asymmetric dc-sources are used (i.e. the dc-link voltages of the various cells are not equal). A general circuit, showing a CHB with k levels can be seen in Figure 24.

The CHB provides a very scalable way to create output signals with very low harmonic content and redundancy especially if a large number of levels are used. Individual cells can be easily replaced, and extra cells can be inserted as stand-by in case they are needed, and activated without user input. The individual power cells can be constructed from low-voltage components. A few industrial suppliers offer this topology, a notable example is the Siemens Sinamics Perfect Harmony line of medium voltage drives.

Drawbacks include a large number of individual components requiring relatively complex real-time calculations for an optimised control strategy. Since each power cell is floating with respect to the others, it could be a challenge to get control power and signals into the cells. In addition, a non-standard multipulse transformer is needed.

3.4.4 Flying capacitor (FLC)

The FLC topology was suggested in the end of the 1990s, and has been implemented by a few producers of medium voltage drives. Compared with the NPC,

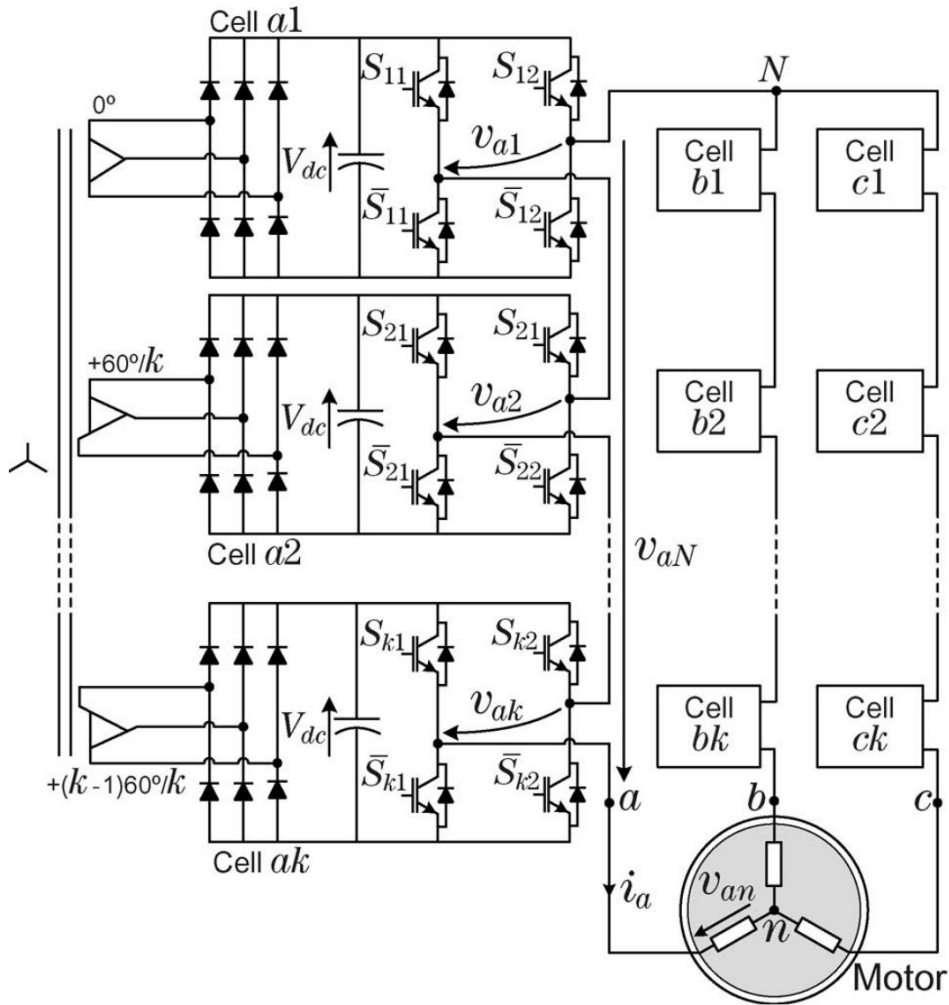


Figure 24: General circuit of the cascaded H-bridge. Picture from [32].

where extra diodes are required to produce the multilevel output, in this configuration there are extra capacitors inserted that provide the clamping feature. An example of a four-level FLC can be seen in Figure 25.

The biggest drawback with this topology is the expense of the additional capacitors, which become especially large at low carrier frequencies (around 1 kHz). One example of an industrial implementation of the flying capacitor topology is the Symphony drive commercialised by ALSTOM (bought by GE in 2015), see [33].

This topology might become even more interesting with the adoption of silicon carbide switches, capable of very high carrier frequencies.

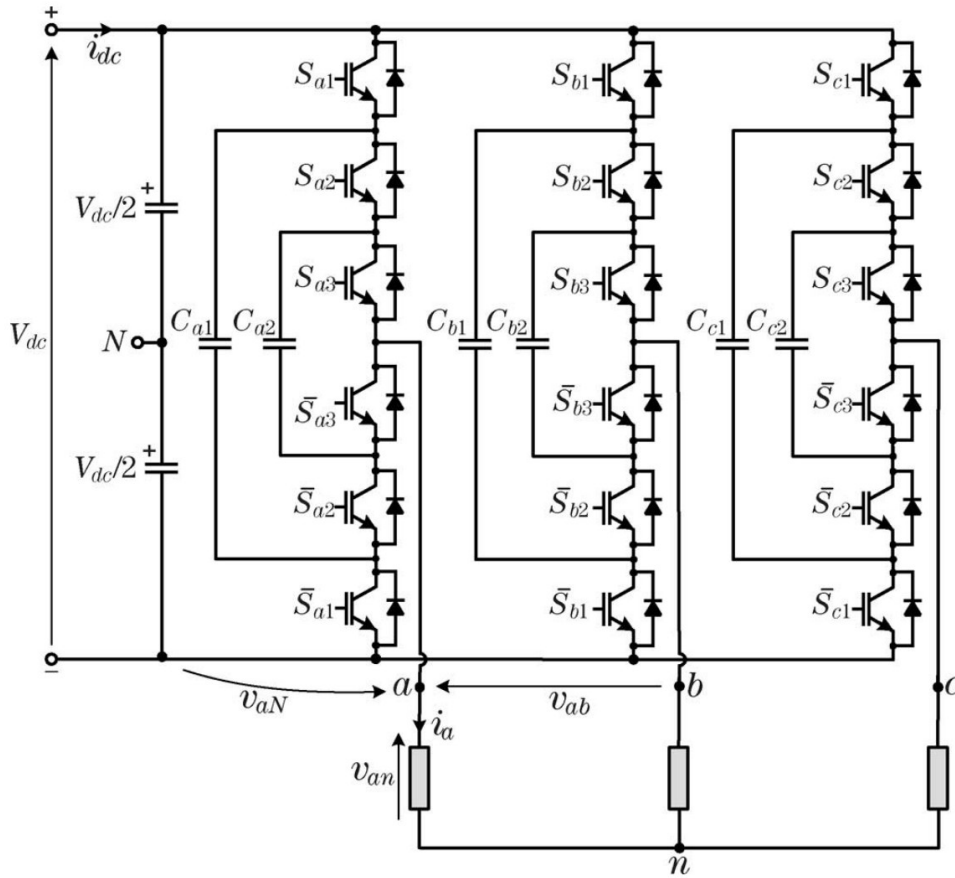


Figure 25: Four-level flying capacitor topology. Picture from [32].

3.4.5 Quantifying the differences

In [34], a quantification of the performance of the three before mentioned topologies under realistic conditions was performed. A design of a 4-kV 4.16 MVA drive using a 3L-NPC, 4L-FLC and a 9L-CHB (among others). The topologies were evaluated based on total losses as well as the expense of components required; switches, capacitors and filter components (sine filter).

The results showed significant differences in the size of the components of the output filter between the different topologies, with the 3L-NPC requiring the biggest filter components and highest amount of installed switch capacity. However, it also highlighted the high extra cost of the additional capacitors needed in the FLC topology.

The 9L-CHB resulted in the lowest amount of installed switch capacity, and also the smallest filter components. However, these advantages come at a cost of a rather complex transformer and complicated control.

3.5 Vector control techniques

Not only the hardware topology matters, but also how the drive is controlled impacts significantly its performance. As a standard, medium voltage drives offer V/f control, where the output voltage is scaled linearly with the mechanical speed of the load. However, also more advanced control techniques are normally offered.

The concept of vector control was first developed for induction motors in the 1970s. This control technique has since then been adopted also by the permanent magnet synchronous machines in various forms.

Two separate control applications exist; inverter control, which generates the current consumed by the load, and AFE control, which controls the active front-end interfacing with the grid. These two applications have different requirements, which in turn has led to differently optimised control strategies. The most common ones are

Field oriented control (FOC, inverter control) This is presently the most widely implemented control technique in industry. In its classical form, it transforms measurements of current from the static reference frame ($\alpha\beta$) to the rotating one (dq) using measurements of rotor angle. In order to achieve maximum torque production, the stator currents are then aligned with the q-axis. The control of the current magnitude is typically achieved using a fixed-frequency PWM signal, with the duty cycle modulated using a PI controller [35].

Direct torque control (DTC, inverter control) This modulation scheme was made popular in particular by ABB in the 1980s. The core of the control system is centered around a digital model of the motor to be controlled. This model takes measurements of the state of the inverter (position of switches, DC-bus voltage) and motor currents as input, and produces estimates of instantaneous flux and torque as outputs. The estimates of flux and torque are fed into a comparator, comparing them with corresponding reference values and finally selecting an optimum state of the inverter. There are no PI regulators, and also no fixed PWM frequency. The dynamic control is very fast with no overshoot in the step-response, but the control requires very high speed processing power (although of very few instructions per cycle) [36], [37].

Voltage-oriented control (VOC, AFE control) The optimization criteria for the control of the AFE is slightly different than that of the load. Typically, the control system aims to keep the DC-link voltage constant while at the same time (ideally) producing sinusoidal input currents of unity power factor. The VOC is the classic solution to this control problem. A measurement

of the DC-link voltage is used as input to the controller, which in turn controls the quadrature component of the current by means of a PI controller. The current is finally implemented by use of a space vector modulator. The similarities between this control and the corresponding version of the FOC are high, with the main difference being that the control signal is dc-link voltage and not speed [38].

Direct-power control (DPC, AFE control) A more recent solution to the same problem is to estimate the flow of power into and out of the system, using a digital model and measured information about the state of the inverter (dc-link voltage, state of the switches), instantaneous line currents and the magnitude of the line reactor. No PI regulators are used in this control scheme, but a bang-bang comparator is used to instantaneously calculate the optimum voltage vector (state of the switches). Also here, there is a strong analog with the DTC motor control, with similar advantages and drawbacks [38].

3.6 Suppliers

The following table lists identified suppliers that offers MV drive systems of at least 6 MW with active front end, that potentially could provide a complete system for the Alpheus project

Company	Semiconductor	Topology	Control	Product name
INGETEAM	IGBT	VSI (3L-NPC)	V/f + Vector	INGEDRIVE MV100
Hitachi	IGCT	VSI (3L-NPC)	MP3C	ACS6080, SS8080
Siemens	IGBT / IGCT	VSI (3L-NPC)	Vector	SM150
AMTECH	IGBT	VSI	Vector	Axpert-Hivert
Toshiba	IEGT	VSI	Vector	T300MV2
Danfoss	IGBT	VSI (3L-NPC)	Vector	VACON 3000
GE	IGBT	VSI	Vector	MV7000
TMEIC	IGBT	VSI	Vector	Tmdrive-50
Fuji Electric	IGBT	VSI	Vector	FRENIC4600

Note that this list is not complete, and further suppliers exist.

3.6.1 INGETEAM

The first supplier on the list (Ingeteam) was contacted in order to get more detailed information regarding the identified product.

Ingeteam is an international technical group specialised in electric power conversion. Its main areas of operation is development of power and control electronics, rotating electric machines, systems and services related to these components. The company has locations in 24 countries and a staff of 4000 [39]. One part of Ingeteam is called Indar and produces hydropower generators up to 100 MV A.

Ingeteam offers a series of drives called Ingedrive, which caters to different power levels and requirements. The product portfolio spans from low-voltage drives with main supply voltages of below 690 V, and output power up to 5.7 MW up to 6.6kV main supply voltage and 44 MW output power. Their drives normally use IGBTs in a 3L-NPC configuration, except for the MV500 (high power, high current) that uses IGCTs, see Figure 26.

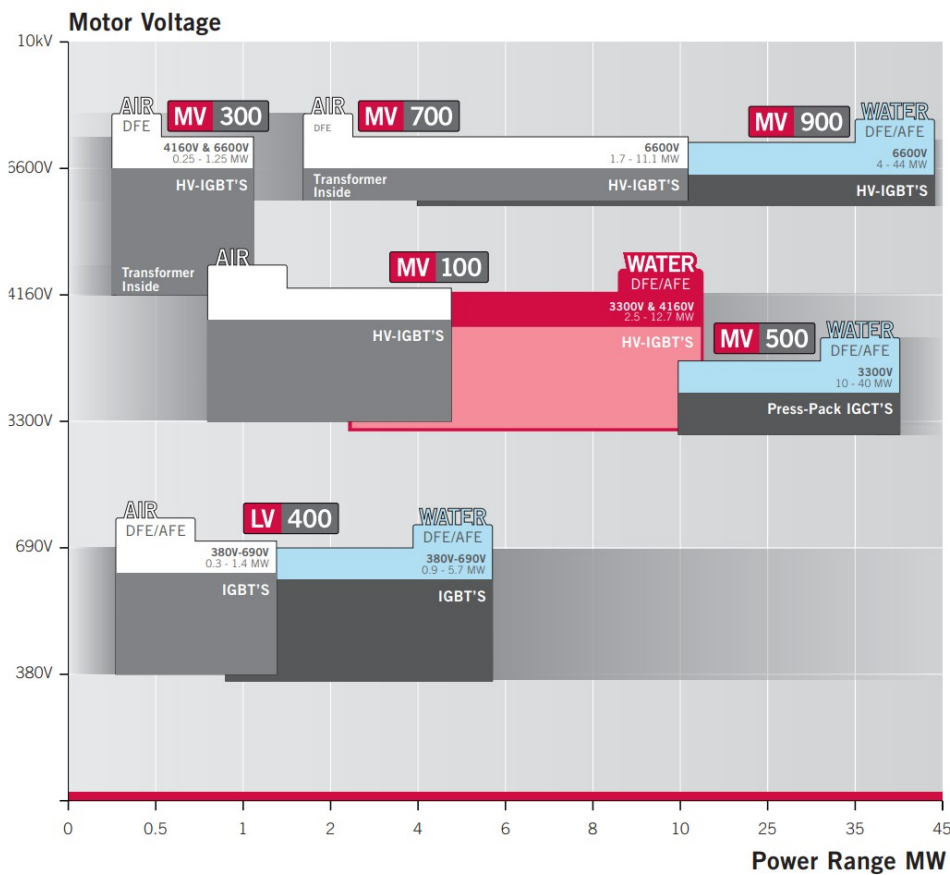


Figure 26: Overview of the INGEDRIVE series. The version suggested by Ingeteam was the MV100 with watercooling [40].

From the requirements of the Alpheus project, the suggestion from the company was to use the Ingedrive 100. The drive comes in two voltage versions (3.3 kV and 4.6 kV) and can be equipped with convective cooling or watercooling. The detailed suggestion from the company was to use two Ingedrive 100 with AFE, each rated for 3.3 kV and with watercooling, connected separately to the grid,

see Figure 27. When using the AFE, the input power factor is 1.

Ingeteam further provides adequately dimensioned input and output filters for the application; LC-filters may be required on the input side, although the THD is typically low when using the optional AFE. On the output side, typically only a dv/dt filter is required for newer electric machines with modern isolation levels while a full sinus-filter is recommended for older machines.

The drive is capable of connecting several electric machines on the same dc-bus. However, the purpose with this set-up is to share power between the machines – if one machine is braking (returning power to the dc-bus) this power should be consumed by the other drive. The rating of the AFE is identical to the output stage and it will not be able to handle the full power from both machines operating as generators at the same time. For this reason, two identical drives (each one connected between the grid and the corresponding electrical machine) is recommended.

The drive can be controlled with the traditional voltage-frequency control, or the more modern vector control. All types of electrical machines can be controlled (asynchronous, PMSM...) and the torque response time is less than 10 ms (from 0% to 100%) with a torque ripple of less than 1%. The AFE is capable of controlling both active and reactive power towards the grid.

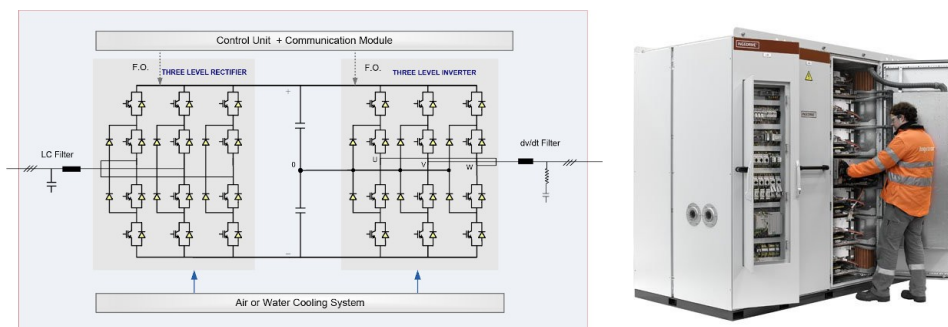


Figure 27: INGEDRIVE MV100: watercooled with active front-end.

In addition to the drive itself, additional components may be required depending on the grid codes

- Switches on the input and output side for maintenance
- Overvoltage limiter unit on the output
- Breaker on the output side

3.6.2 Conclusion

From the investigation into existing technologies for medium voltage drives, it can be seen that commercial off-the-shelf solutions are readily available that would fulfill the needs of the Alpheus project.

The investigated drives typically have a response time of less than 10 ms and most of them use an IGBT based system in a multilevel configuration with active front-end.

Many suppliers offer the possibility to connect two or more electric machines on the same DC-bus, but they do normally not dimension the AFE considering full generating power, since they typically do this in order to allow machines to share power - when one device is acting as a generator they assume another one is acting as a motor.

References

- [1] D. Truijen, “20220323_ALPHEUS_WP3_FCRimplementation_SurrogateModel,” tech. rep., ALPHEUS, 2022. URL.
- [2] J. Abrahamsson, “20220323_ALPHEUS_WP3_FCRimplementation_FatigueAnalysis,” tech. rep., ALPHEUS, 2022. URL.
- [3] M. Qudaih and B. Engel, “FCR profile dataset is derived from historic frequency data for further use in WP3,” tech. rep., ALPHEUS, 2021. URL.
- [4] D. Truijen and J. D. Kooning, “Deliverable 3.1: Control concepts for power reference tracking,” tech. rep., ALPHEUS, 2021. URL.
- [5] H. Abu-Rub, S. Bayhan, S. Moinoddin, M. Malinowski, and J. Guzinski, “Medium-voltage drives: Challenges and existing technology,” *IEEE Power Electronics Magazine*, vol. 3, no. 2, pp. 29–41, 2016.
- [6] M. Hiller, R. Sommer, and M. Beuermann, “Medium-voltage drives,” *IEEE Industry applications magazine*, vol. 16, no. 2, pp. 22–30, 2010.
- [7] D. P. Truijen, J. D. De Kooning, and K. Stockman, “Drivetrain architectures for a mechanically decoupled contra-rotating reversible pump-turbine,” in *2021 IEEE/ASME International Conference on Advanced Intelligent Mechatronics (AIM)*, pp. 7–12, IEEE, 2021.
- [8] “Acs6080 user manual.” <https://search.abb.com/library/Download.aspx?DocumentID=3BHS842007%20E01&LanguageCode=en&DocumentPartId=&Action=Launch>. Accessed: 2021-10-14.
- [9] G. L. Arsov and S. Mirčevski, “The sixth decade of the thyristor,” *FACULTY OF ELECTRICAL ENGINEERING UNIVERSITY OF BANJA LUKA*, p. 3, 2010.
- [10] “Medium voltage drive evolution.” <https://www.tmeic.com/medium-voltage-drive-evolution>. Accessed: 2021-09-21.
- [11] R. Van Ligten and D. Navon, “Base turn-off of pnpn switches,” in *IRE WES-CON Convention Record, Part*, vol. 3, pp. 49–52, 1960.
- [12] “Feature and application of gate turn-off thyristors.” <https://www.mitsubishielectric.com/semiconductors/files/manuals/gtothyristors.pdf>. Accessed: 2021-10-04.
- [13] N. Iwamuro and T. Laska, “Igbt history, state-of-the-art, and future prospects,” *IEEE Transactions on Electron Devices*, vol. 64, no. 3, pp. 741–752, 2017.
- [14] H. Chang, B. Baliga, J. Kretchmer, and P. Piacente, “Insulated gate bipolar transistor (igbt) with a trench gate structure,” in *1987 International Electron Devices Meeting*, pp. 674–677, IEEE, 1987.

- [15] M. Kitagawa, I. Omura, S. Hasegawa, T. Inoue, and A. Nakagawa, "A 4500 v injection enhanced insulated gate bipolar transistor (iegt) operating in a mode similar to a thyristor," in *Proceedings of ieee international electron devices meeting*, pp. 679–682, IEEE, 1993.
- [16] T. Laska, M. Munzer, F. Pfirsch, C. Schaeffer, and T. Schmidt, "The field stop igbt (fs igbt). a new power device concept with a great improvement potential," in *12th International Symposium on Power Semiconductor Devices & ICs. Proceedings (Cat. No. 00CH37094)*, pp. 355–358, IEEE, 2000.
- [17] "Hvigt modules." <https://www.mitsubishielectric.com/semiconductors/products/powermod/hvigtmod/index.html>. Accessed: 2021-09-10.
- [18] "Igbt modules." <https://www.infineon.com/cms/en/product/power/igbt/igbt-modules/>. Accessed: 2021-09-10.
- [19] "Hitachi igbt status list." https://www.hitachi-power-semiconductor-device.co.jp/en/products/igbt/pdf/ig13_eR3_2021_07.pdf. Accessed: 2021-09-10.
- [20] "Cm1800hc-66x." https://www.mitsubishielectric.com/semiconductors/content/product/powermodule/hvigt_ipm/x_series/cm1800hc-66x_e.pdf. Accessed: 2021-09-30.
- [21] R. Kamibaba and N. Morimoto, "7th generation power chip technologies for industrial application," *Mitsubishi Electric ADVANCE*, 2016.
- [22] P. Steimer, O. Apeldoorn, E. Carroll, and A. Nagel, "Igct technology baseline and future opportunities," in *2001 IEEE/PES Transmission and Distribution Conference and Exposition. Developing New Perspectives (Cat. No. 01CH37294)*, vol. 2, pp. 1182–1187, IEEE, 2001.
- [23] P. K. Steimer, H. Gruning, J. Werninger, E. Carroll, S. Klaka, and S. Linder, "Igct-a new emerging technology for high power, low cost inverters," in *IAS'97. Conference Record of the 1997 IEEE Industry Applications Conference Thirty-Second IAS Annual Meeting*, vol. 2, pp. 1592–1599, IEEE, 1997.
- [24] C. Thomas and B. Björn, "High power igct switches-state-of-the-art and future," in *Issue 3 2011 Power Electronics Europe PCIM*, pp. 30–34, 2011.
- [25] "Asymmetric integrated gatecommutated thyristor 5shy 65l4521." <https://search.abb.com/library/Download.aspx?DocumentID=5SYA1261&LanguageCode=en&DocumentPartId=&Action=Launch>. Accessed: 2021-10-04.
- [26] P. Seidenberg, "From germanium to silicon: A history of change in the technology of the semiconductors," *Facets: New perspectives on the history of semiconductors*, pp. 35–74, 1997.

- [27] “Comparison of sic mosfet and si igbt.” <https://toshiba.semicon-storage.com/info/docget.jsp?did=69799>. Accessed: 2021-10-13.
- [28] M. Nitzsche, C. Cheshire, M. Fischer, J. Ruthardt, and J. Roth-Stielow, “Comprehensive comparison of a sic mosfet and si igbt based inverter,” in *PCIM Europe 2019; International Exhibition and Conference for Power Electronics, Intelligent Motion, Renewable Energy and Energy Management*, pp. 1–7, VDE, 2019.
- [29] T. Ziemann, U. Grossner, and J. Neuenschwander, “Power cycling of commercial sic mosfets,” in *2018 IEEE 6th Workshop on Wide Bandgap Power Devices and Applications (WiPDA)*, pp. 24–31, IEEE, 2018.
- [30] “High-power electric solutions.” <https://toshiba.semicon-storage.com/info/docget.jsp?did=15673>. Accessed: 2021-10-14.
- [31] A. Sugiyama, H. Okitsu, T. Ishimaru, Y. Kishimoto, S. Kadooka, and T. Sawakami, “Verification tests of 3.3 kv sic (silicon carbide) hybrid igbt inverter for nishi-nippon railroad co., ltd 3000 series,” in *2015 International Conference on Electrical Systems for Aircraft, Railway, Ship Propulsion and Road Vehicles (ESARS)*, pp. 1–4, IEEE, 2015.
- [32] J. Rodríguez, S. Bernet, B. Wu, J. O. Pontt, and S. Kouro, “Multilevel voltage-source-converter topologies for industrial medium-voltage drives,” *IEEE Transactions on industrial electronics*, vol. 54, no. 6, pp. 2930–2945, 2007.
- [33] T. A. Meynard, H. Foch, P. Thomas, J. Courault, R. Jakob, and M. Nahrstaedt, “Multicell converters: basic concepts and industry applications,” *IEEE transactions on industrial electronics*, vol. 49, no. 5, pp. 955–964, 2002.
- [34] S. S. Fazel, S. Bernet, D. Krug, and K. Jalili, “Design and comparison of 4-kv neutral-point-clamped, flying-capacitor, and series-connected h-bridge multilevel converters,” *IEEE Transactions on Industry Applications*, vol. 43, no. 4, pp. 1032–1040, 2007.
- [35] V. M. Bida, D. V. Samokhvalov, and F. S. Al-Mahturi, “Pmsm vector control techniques—a survey,” in *2018 IEEE Conference of Russian Young Researchers in Electrical and Electronic Engineering (EIConRus)*, pp. 577–581, IEEE, 2018.
- [36] P. Tiitinen and M. Surandra, “The next generation motor control method, dtc direct torque control,” in *Proceedings of International Conference on Power Electronics, Drives and Energy Systems for Industrial Growth*, vol. 1, pp. 37–43, IEEE, 1996.

- [37] J. N. Nash, "Direct torque control, induction motor vector control without an encoder," *IEEE Transactions on industry applications*, vol. 33, no. 2, pp. 333–341, 1997.
- [38] M. Malinowski, M. P. Kazmierkowski, and A. M. Trzynadlowski, "A comparative study of control techniques for pwm rectifiers in ac adjustable speed drives," *IEEE Transactions on power electronics*, vol. 18, no. 6, pp. 1390–1396, 2003.
- [39] "About us." <https://www.ingeteam.com/en-us/aboutus/ingeteam.aspx>. Accessed: 2021-10-27.
- [40] "Frequency converters / ingedrive mv100." https://www.ingeteam.com/en-us/power-electronics/power-converters/pc28_6_172/ingedrive-mv100.aspx. Accessed: 2021-10-27.